

Supporting information for:

A Pencil-and-Paper Method for Elucidating Halide Double Perovskite Band Structures

Adam H. Slavney,[†] Bridget A. Connor,[†] Linn Leppert,[‡] Hemamala I. Karunadasa^{†,#,*}

[†]Department of Chemistry, Stanford University, Stanford, California 94305, United States

[‡]Institute of Physics, University of Bayreuth, 95440 Bayreuth, Germany

[#]Stanford Institute for Materials and Energy Sciences, SLAC National Accelerator Laboratory, Menlo Park, California 94025, United States

*hemamala@stanford.edu

Table of contents:

Overview of the linear combination of atomic orbitals (LCAO) method

Computational methods

Octahedral molecular orbital diagram (Figure S1)

Geometric details and transformations of the double perovskite unit cell (Figure S2)

Discussion of relativistic effects (Figure S3)

Discussion of σ -bonding bands

Derivation of the σ -bonding SALCs (Figure S4)

Halide-only Bloch waves derived from σ -bonding SALCs (Figures S5 – S17)

Analysis of halide-halide interactions (Figure S18)

Discussion of π -bonding bands

Derivation of π -bonding SALCs (Figures S19-S20)

Halide-only Bloch waves derived from π -bonding SALCs (Figure S21 – S22)

Halide-halide interactions in a π -bonding Bloch wave (Figure S23)

Predictions of band extrema in π -bonding bands (Table S1)

Discussion of Cs₂NaBiCl₆

Band structures of Cs₂NaBiCl₆ and Cs₂KBiCl₆ (Figure S24 – S25)

Overview of the Linear Combination of Atomic Orbitals (LCAO) Method

The atomistic origin of electronic bands in solids is an established theory in solid-state chemistry and physics and the subject of many excellent texts.¹ We briefly review it here. We use a qualitative Linear Combination of Atomic Orbitals (LCAO) method to develop our picture of electronic bands (Figure 2). This model assumes that the electronic states of the solid will be some linear combination of the atomic orbitals of all the constituent atoms. This is exactly equivalent to the Molecular Orbital (MO) theory familiar to most molecular chemists. In MO theory, we combine the ligands to form symmetry-adapted linear combinations (SALCs) based on the point symmetry of the molecule. Similarly, we will begin by finding SALCs of the six σ -bonding halide p orbitals present in the double perovskite unit cell, based on their octahedral point symmetry. Unlike molecules that possess only point symmetry, extended solids also display translational symmetry, which propagates the unit cell through translations along the three unit-cell axes. Following our construction of the SALCs, we must then go beyond MO theory by introducing these additional translational symmetry elements. We do this by tessellating our SALCs from unit cell to unit cell across the crystal lattice. The resulting electronic states are called Bloch waves because the SALCs form a set of periodic patterns that run along various directions in the lattice. Mathematically, translation of the halide SALCs requires the introduction of a new quantum number, \mathbf{k} , which describes how the phases of the halide SALCs change upon translation. Each value of \mathbf{k} corresponds to a different Bloch wave with a different periodicity/spatial frequency. Although \mathbf{k} can hold a wide range of values, we focus on specific values of \mathbf{k} where all unit cells are either perfectly in phase or out of phase with the origin. These values of \mathbf{k} are called high-symmetry \mathbf{k} points and are usually extrema or inflection points within an electronic band because every unit cell is fully involved in the electronic state. By focusing on these high-symmetry \mathbf{k} points, we can generally find the most important points in each band. Other values of \mathbf{k} typically interpolate between the high-symmetry \mathbf{k} points.

Once we have found halide-only Bloch waves at each high-symmetry \mathbf{k} point, we return to MO theory to evaluate their interactions with the central metal orbitals. For some of these Bloch waves, the symmetry of the surrounding halide ligands will match that of the metal cation orbitals, and they will interact to form bonding and antibonding combinations with lower and higher energies, respectively. Other Bloch waves will have mismatched symmetry and show non-bonding interactions with the metal orbitals. After evaluating the bonding/antibonding/non-bonding character of the metal orbitals with each Bloch wave, we can qualitatively rank their relative energies. Plotting these energies versus \mathbf{k} and interpolating between them allows us to construct a band diagram (such as is produced in a DFT calculation) which can be used to determine if the bandgap is direct or indirect, symmetry-allowed or symmetry-forbidden.

Computational Methods

Our first principles density functional theory (DFT) calculations were performed using the Vienna Ab Initio Simulation Package (VASP).² We used the exchange-correlation approximation PBEsol³ to relax the geometries of $\text{Cs}_2\text{AgBiBr}_6$, Cs_2SnBr_6 , and $\text{Cs}_2\text{NaBiCl}_6$, resulting in lattice parameters of 11.19 Å, 10.82 Å, and 10.78 Å, in good agreement with the experimental values of 11.25 Å,⁴ 10.77 Å,⁵ and 10.84 Å,⁶ respectively. The Brillouin zone integrations were performed on a grid of $4 \times 4 \times 4$ \mathbf{k} -points, with a cutoff energy for the plane wave expansion of 600 eV and forces were relaxed until smaller than 0.0001 eV/Å. Projector Augmented Wave (PAW) potentials⁷ were used

with the following valence configurations: Cs: $5s^25p^66s^1$, Ag $4d^{10}5s^1$, Bi $6s^26p^3$, Br $4s^24p^5$, Cl $3s^23p^5$, Sn $5s^25p^2$, and Na $3s^1$.

For band structure calculations, we used the same exchange-correlation functional and included spin-orbit coupling self-consistently, using a plane wave energy cutoff of 500 eV. Atomic orbital contributions at each \mathbf{k} -point were obtained by projecting PBEsol+SOC Kohn-Sham orbitals onto spherical harmonics within spheres centered at each ion.

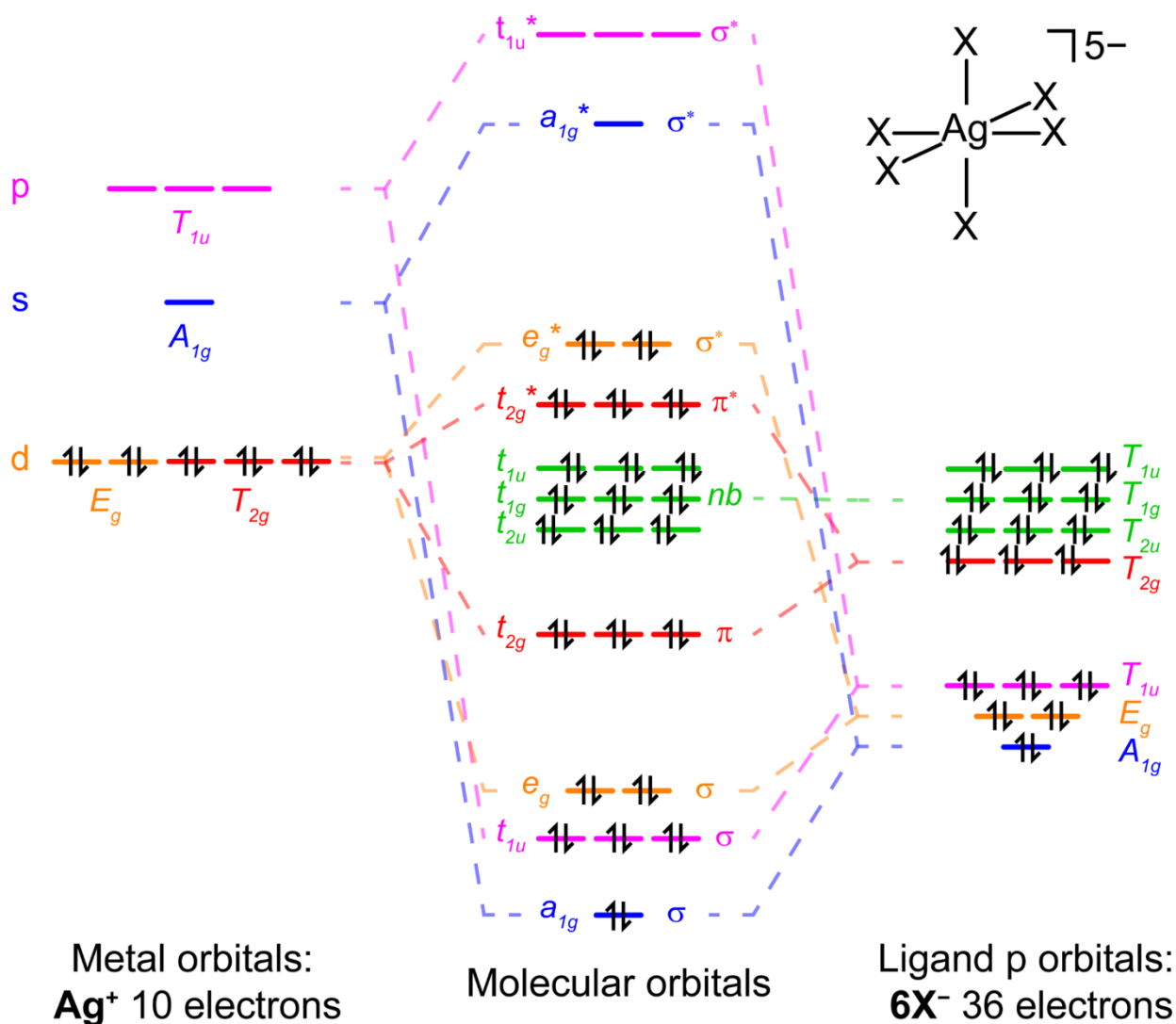


Figure S1. General molecular-orbital diagram for a molecular metal-hexahalide octahedral complex. The A_{1g} and E_g ligand sets are σ -bonding, the T_{2g} set is π -bonding and the T_{1g} and T_{2u} sets are non-bonding. T_{1u} has two sets; one σ and one nonbonding. The exact electronic configuration shown is for Ag^+ but the electronic configuration of any other octahedral ion can be obtained by adding or subtracting the appropriate number of electrons.

Geometric Details of the Double Perovskite Unit Cell

The conventional cubic cell of the $Fm\bar{3}m$ double perovskite shows the face-centered-cubic symmetry of the lattice and contains four formula units (black lines in Figure S2). It is possible to find a smaller rhombohedral cell (red lines in Figure S2A & C) which contains only one formula unit and is the unit cell of the lattice. The axes of the rhombohedral cell (\mathbf{a}_1 , \mathbf{a}_2 , \mathbf{a}_3) are oriented along the face-diagonals of the cubic cell and are angled at 60° from one another. The high-symmetry \mathbf{k} points of the double perovskite structure are defined with respect to the rhombohedral cell and we utilize this cell exclusively for all of our analysis.

To make the double perovskite translational symmetry easier to visualize, we project the rhombohedral unit-cell vectors onto a Cartesian plane. One rhombohedral vector (\mathbf{a}_1) runs diagonally along the Cartesian xz plane. The difference between the remaining two rhombohedral vectors ($\mathbf{a}_2 - \mathbf{a}_3$) gives another vector that also runs diagonally along the Cartesian xz plane at a 90° angle from the \mathbf{a}_1 vector (Figure S2B & D). Thus, we can combine the three values stored in \mathbf{k} as two orthogonal vectors in the Cartesian xz plane, as in Figure 4. The Cartesian xy and yz planes can be expressed similarly using different combinations of the rhombohedral axes.

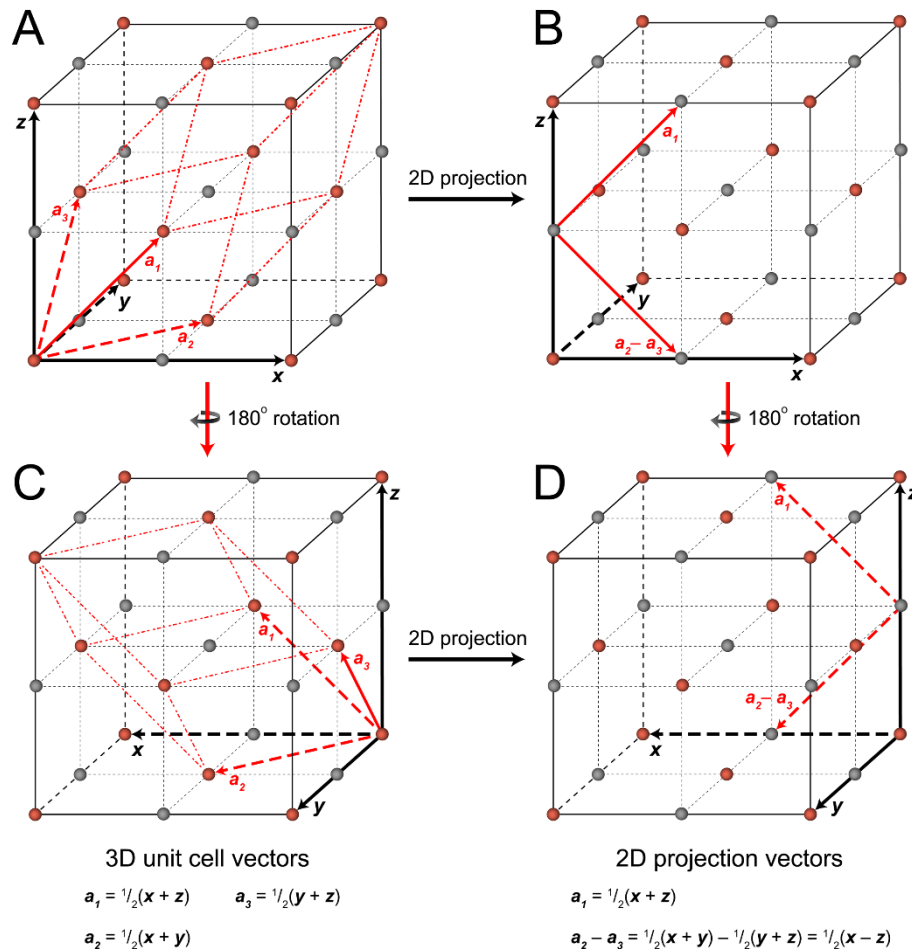


Figure S2. A) Symmetry relations between the conventional (black) and rhombohedral (red) double perovskite cells. The conventional cell vectors are \mathbf{x} , \mathbf{y} , and \mathbf{z} and the rhombohedral unit-cell vectors are \mathbf{a}_1 , \mathbf{a}_2 , and \mathbf{a}_3 . **B)** Projection of the rhombohedral vectors onto the xz -plane to give two orthogonal vectors used to construct Bloch waves. **C)** and **D)** Alternative perspectives of **A** and **B**. Orange and grey spheres represent the B and B' atoms, respectively.

Relativistic Effects

The theory we have developed in the main text is a nonrelativistic one, and it does not account for the effects of spin-orbit coupling (SOC) on the band structure. Despite this, we obtain remarkable correspondence between our predictions and DFT calculations, which include spin-orbit coupling, even in compounds with heavy elements where relativistic effects are known to be significant. In general, SOC can be viewed as a relatively small perturbation to the overall energy of the electronic states. The primary effects of this perturbation are additional splitting of nominally degenerate bands derived from p and d orbitals. The relative dispersion of each band is also affected to a lesser extent.

A comparison of the DFT band structure of $\text{Cs}_2\text{AgBiBr}_6$, our first case study, with and without spin-orbit coupling provides an excellent example of this (Figure S3). Without spin-orbit coupling, our LCAO method exactly reproduces the energetic ordering and degeneracies of the conduction and valence bands. However, inclusion of spin-orbit coupling results in a small splitting of the valence bands near L and a larger splitting of the conduction band into $p_{1/2}$ and $p_{3/2}$ branches at all \mathbf{k} points. More significant effects are observed in the conduction band, consistent with greater participation of orbitals from the heavier Bi^{3+} cation in those states.

The remarkable concurrence we see between our predictions and relativistic DFT calculations can be attributed to the relatively small effect SOC has on band dispersion. For compounds with reasonably dispersive bands the differences in energy between high-symmetry \mathbf{k} points tend to be greater than the SOC perturbation. Indeed, for all the 3D double perovskites we have examined here, inclusion of spin-orbit coupling does not change the position of the VBM and CBM. This will not always be the case, particularly for materials with very flat bands. For example, in the 2D double perovskite $(\text{BA})_4\text{AgBiBr}_8$ ($\text{BA} = n$ -butylammonium), spin-orbit coupling plays a key role in generating the material's direct bandgap.⁸

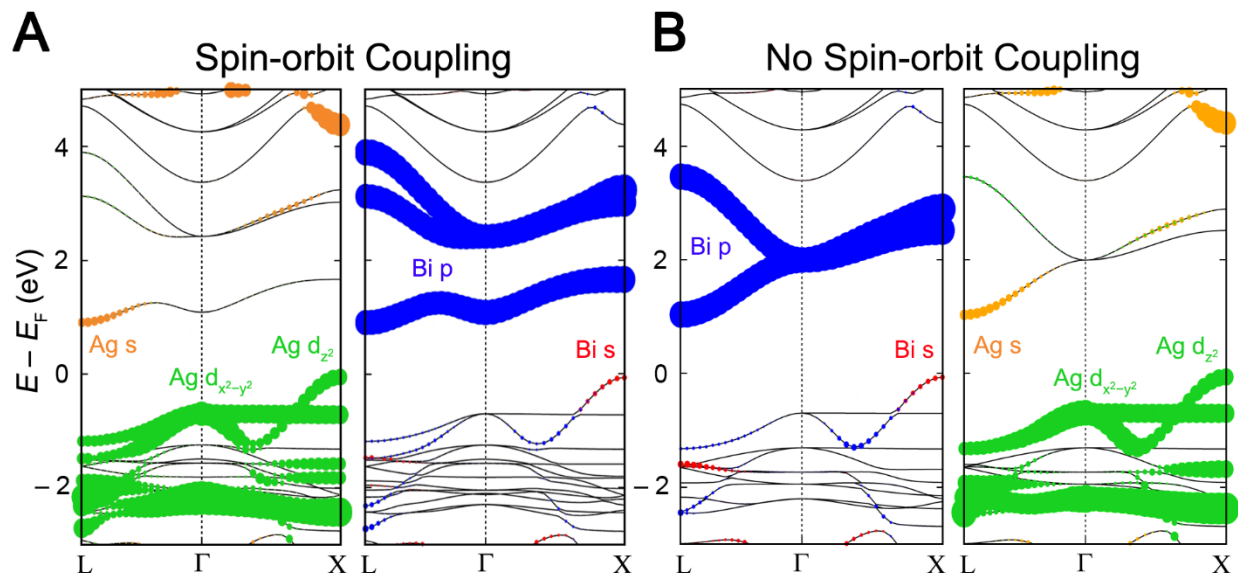


Figure S3. Band structure of the double perovskite $\text{Cs}_2\text{AgBiBr}_6$ computed by DFT with **A)** spin-orbit coupling included and **B)** spin-orbit coupling omitted. The band structures are shown in duplicate and the orbital contributions of the B-site atoms (Ag and Bi) are given in color with the size of the dots proportional to the size of the contribution. Halide contributions are also present but have been omitted for clarity.

Discussion of σ -bonding bands

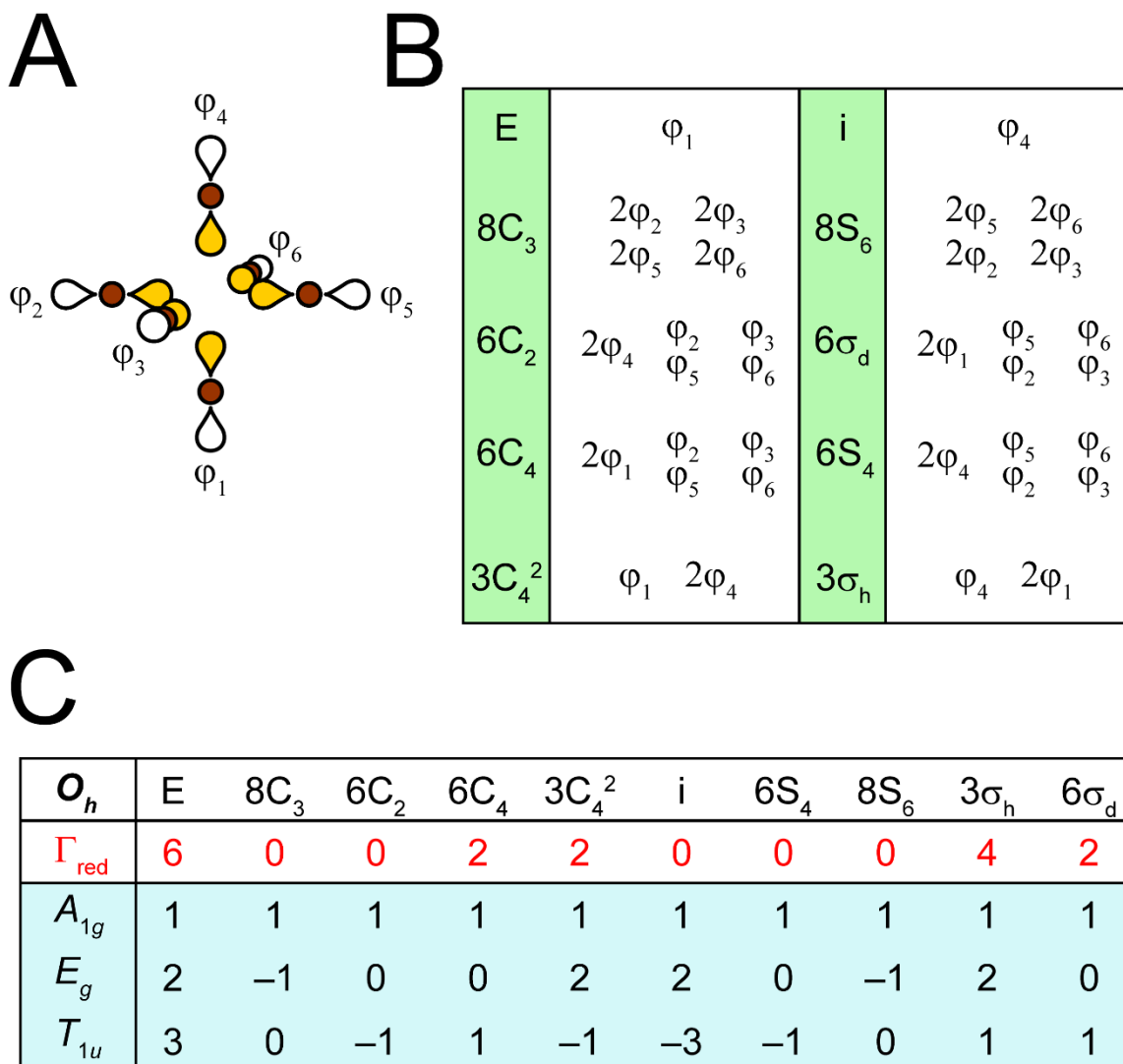


Figure S4. **A)** The octahedral arrangement of halide p orbitals, present in the double perovskite unit cell, used to construct the σ -bonding SALCs. **B)** Projection table based on orbital φ_1 showing its relationship to the other orbitals in **A** under the symmetry operations of the O_h point group (green columns). **C)** Decomposition of the reducible representation for the orbitals in **A** into their irreducible representations (A_{1g} , E_g , & T_{1u}).

Derivation of σ -bonding SALCs

To construct σ -bonding SALCs, we consider the six halide p orbitals within the rhombohedral unit cell that point directly at the B site and which overall have O_h point symmetry. Figure S4A defines our labeling scheme for these six orbitals. Figure S4C gives the reducible representation (Γ_{red}) generated by observing how many of these six orbitals remain unchanged under each symmetry operation. Γ_{red} can be decomposed into the sum of three irreducible representations, $A_{1g} + T_{1u} + E_g$, which will define the symmetry of our SALCs. The SALCs for each irreducible representation, shown in Figure 2, were found using the projection operator. The projection operator takes the character (χ_j) of each symmetry operation in the irreducible representation and multiplies it by the projection table entry (p_j) for that operation.

$$\mathbf{P}_i(\varphi_x) = \frac{1}{N} \sum \chi_j \times p_j \quad (1)$$

The projection table for φ_1 is given in Figure S4B. This table is obtained by determining which halide p orbital φ_1 maps onto under each symmetry operation (for example, under the eight C_3 rotation operators, φ_1 maps onto $\varphi_2, \varphi_3, \varphi_5,$ and φ_6). The normalization factor, N , is defined as follows:

$$N = \sqrt{\sum (c_x)^2} \quad (2)$$

where c_x is the coefficient for each φ_x after application of the projection operator. The SALC for A_{1g} can be determined through direct application of the projection operator

$$\mathbf{P}_{A_{1g}}(\varphi_1) = \frac{1}{\sqrt{6}}(\varphi_1 + \varphi_2 + \varphi_3 + \varphi_4 + \varphi_5 + \varphi_6) \quad (3)$$

One of the two SALCs of the E_g representation can likewise be determined directly

$$\mathbf{P}_{E_g}(\varphi_1) = \frac{1}{2\sqrt{3}}(2\varphi_1 - \varphi_2 - \varphi_3 + 2\varphi_4 - \varphi_5 - \varphi_6) \quad (4)$$

The other E_g SALC may be found from a linear combination of $\mathbf{P}_{E_g}(\varphi_2)$ and $\mathbf{P}_{E_g}(\varphi_3)$

$$\frac{1}{N}[\mathbf{P}_{E_g}(\varphi_2) - \mathbf{P}_{E_g}(\varphi_3)] = \frac{1}{2}(\varphi_2 - \varphi_3 + \varphi_5 - \varphi_6) \quad (5)$$

where

$$\mathbf{P}_{E_g}(\varphi_2) = \frac{1}{2\sqrt{3}}(-\varphi_1 + 2\varphi_2 - \varphi_3 - \varphi_4 + 2\varphi_5 - \varphi_6) \quad (6)$$

$$\mathbf{P}_{E_g}(\varphi_3) = \frac{1}{2\sqrt{3}}(-\varphi_1 - \varphi_2 + 2\varphi_3 - \varphi_4 - \varphi_5 + 2\varphi_6) \quad (7)$$

Similarly, the first T_{1u} SALC is found directly

$$\mathbf{P}_{T_{1u}}(\varphi_1) = \frac{1}{\sqrt{2}}(\varphi_1 - \varphi_4) \quad (8)$$

while the other two T_{1u} SALCs are found by changing the starting orbital:

$$\mathbf{P}_{T_{1u}}(\varphi_2) = \frac{1}{\sqrt{2}}(\varphi_2 - \varphi_5) \quad (9)$$

$$\mathbf{P}_{T_{1u}}(\varphi_3) = \frac{1}{\sqrt{2}}(\varphi_3 - \varphi_6) \quad (10)$$

Halide-only Bloch waves derived from σ -bonding SALCs

As discussed in main text Section 2.3, there are 11 non-degenerate Bloch waves at the three high-symmetry \mathbf{k} points: 3 each at Γ and \mathbf{L} and 5 at \mathbf{X} . The following 13 figures (Figures S5 – S17) depict each of these Bloch waves. For ease of visualization, we have chosen to show the doubly degenerate E_g set in two separate figures at the isotropic \mathbf{k} points Γ and \mathbf{L} . The triply degenerate T_{1u} set is shown together at the Γ and \mathbf{L} points. At the anisotropic \mathbf{k} point \mathbf{X} , the degeneracy of both the E_g and T_{1u} sets is reduced. The T_{1u} set splits into a doubly degenerate and a singly degenerate representation while the E_g set splits into two non-degenerate representations. All four non-degenerate representations are shown in separate figures (Figures S14 – S17).

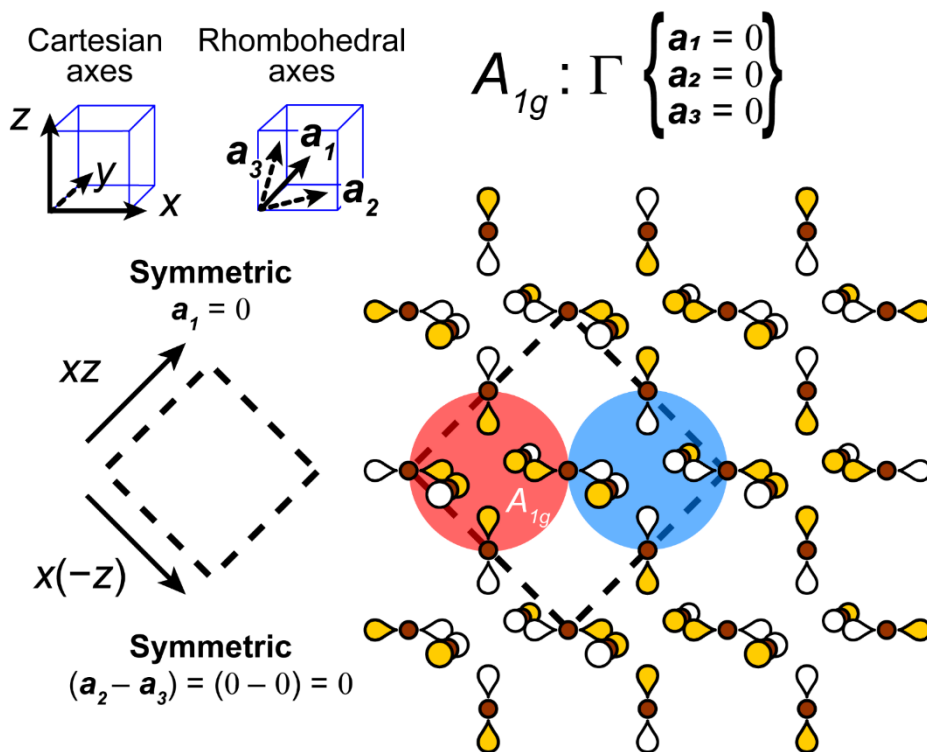


Figure S5. Derivation of the Bloch wave at Γ derived from the A_{1g} SALC (red circle).

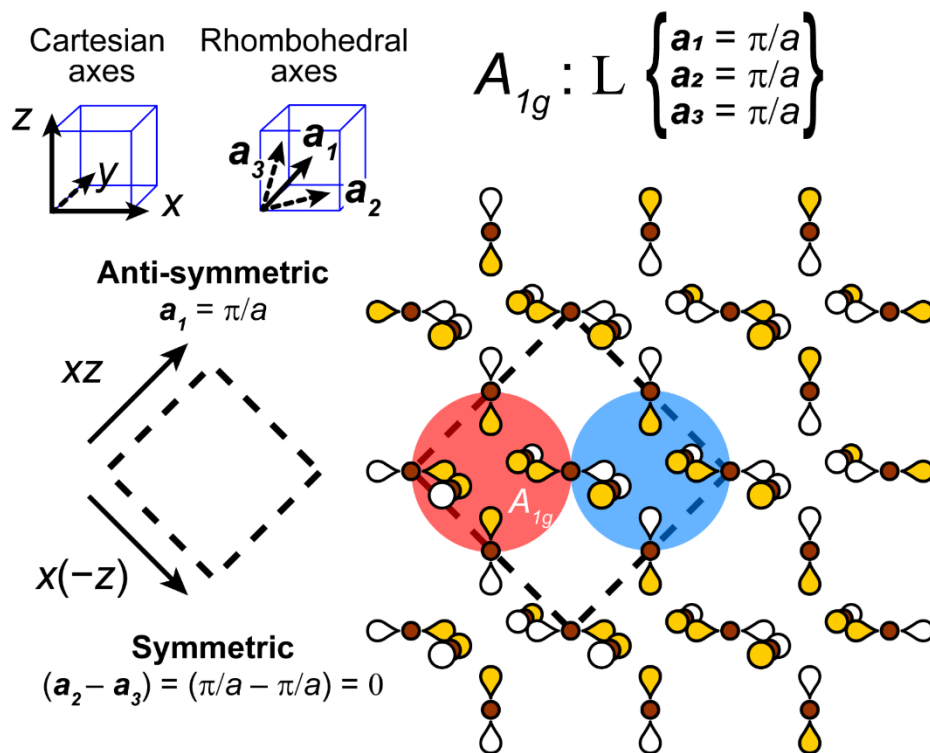


Figure S6. Derivation of the Bloch wave at L derived from the A_{1g} SALC (red circle).

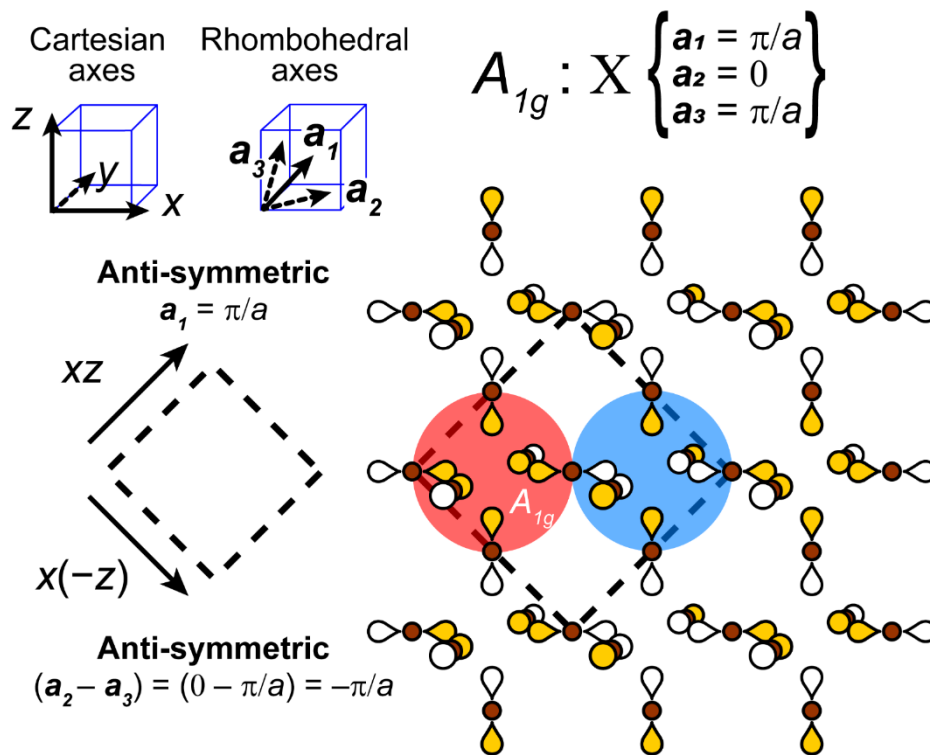


Figure S7. Derivation of the Bloch wave at X derived from the A_{1g} SALC (red circle).

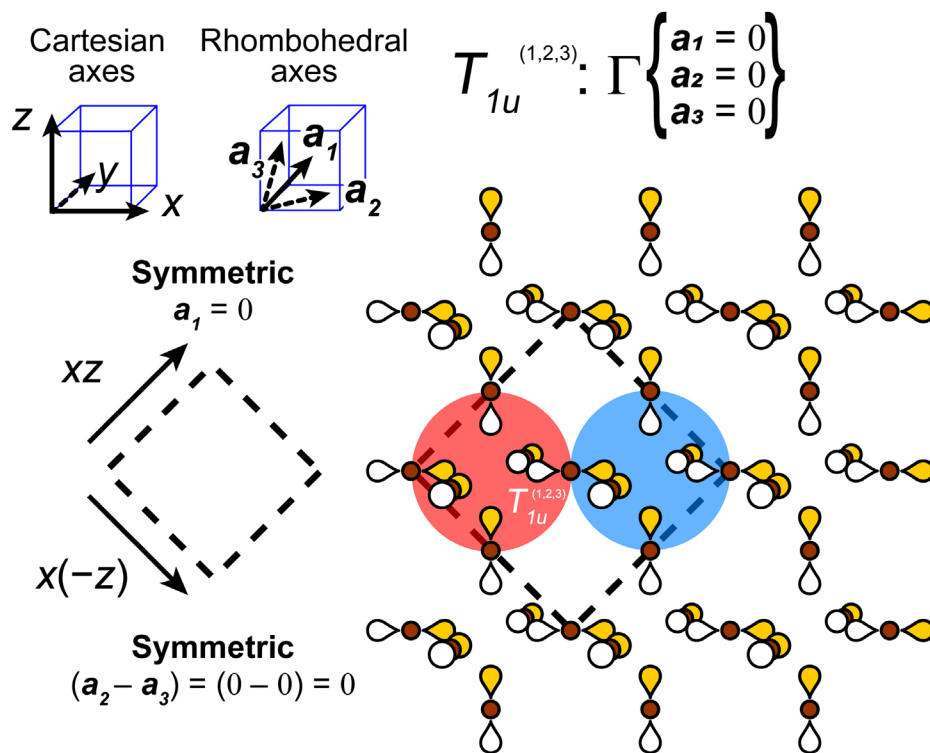


Figure S8. Derivation of the Bloch wave at Γ derived from the T_{1u} SALCs (red circle). All three degenerate SALCs ($T_{1u}^{(1)}$, $T_{1u}^{(2)}$, and $T_{1u}^{(3)}$) are shown.

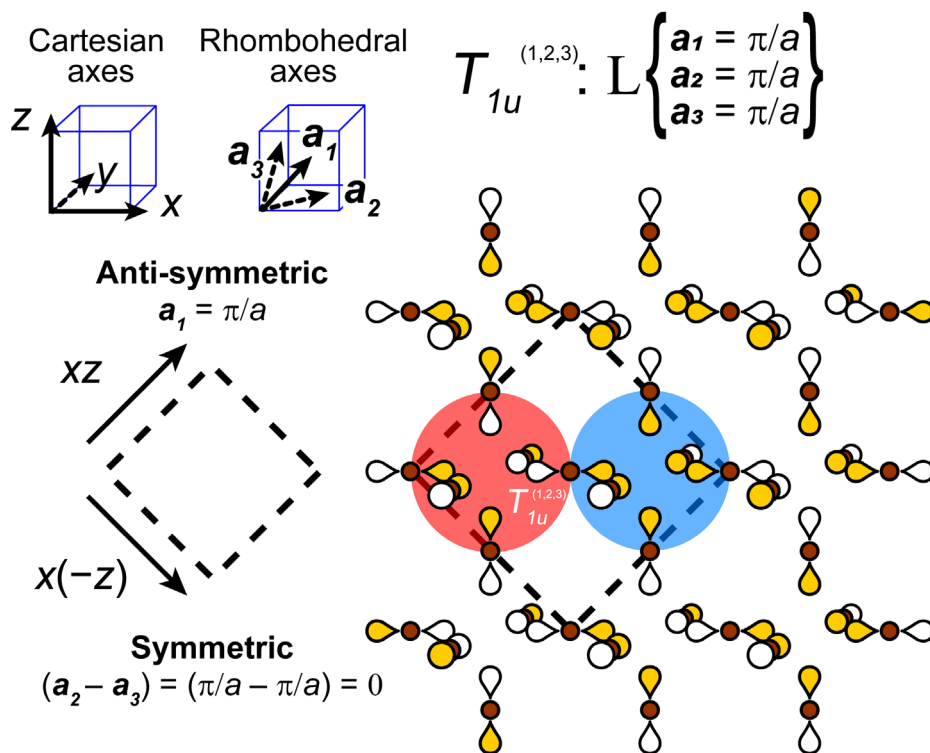


Figure S9. Derivation of the Bloch wave at L derived from the T_{1u} SALCs (red circle). All three degenerate SALCs ($T_{1u}^{(1)}$, $T_{1u}^{(2)}$, and $T_{1u}^{(3)}$) are shown.

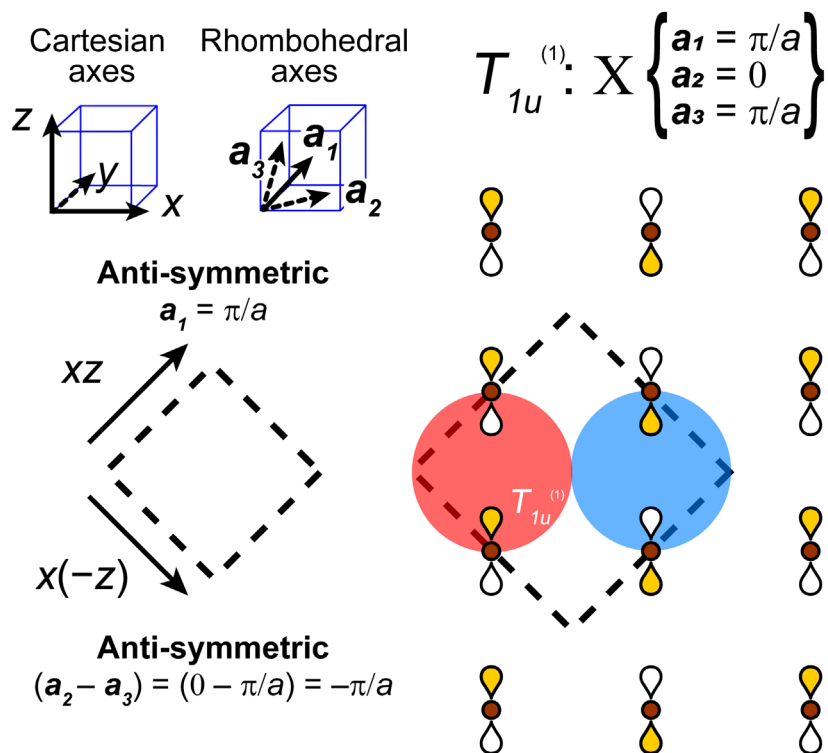


Figure S10. Derivation of the Bloch wave at X derived from the T_{1u} SALC. The anisotropic translational symmetry at X splits the T_{1u} into singly and doubly degenerate sets. Only the singly degenerate SALC ($T_{1u}^{(1)}$) is shown.

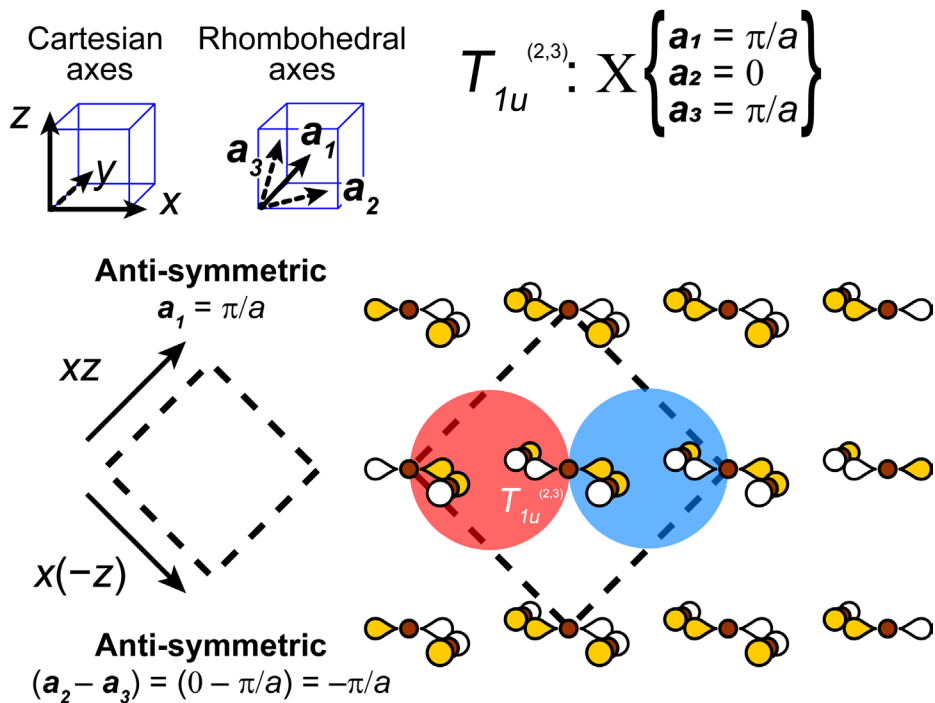


Figure S11. Derivation of the Bloch wave at X derived from the T_{1u} SALC (red circle). The anisotropic translational symmetry at X splits the T_{1u} into singly and doubly degenerate sets. Only the doubly degenerate SALCs ($T_{1u}^{(2)}$ and $T_{1u}^{(3)}$) are shown.

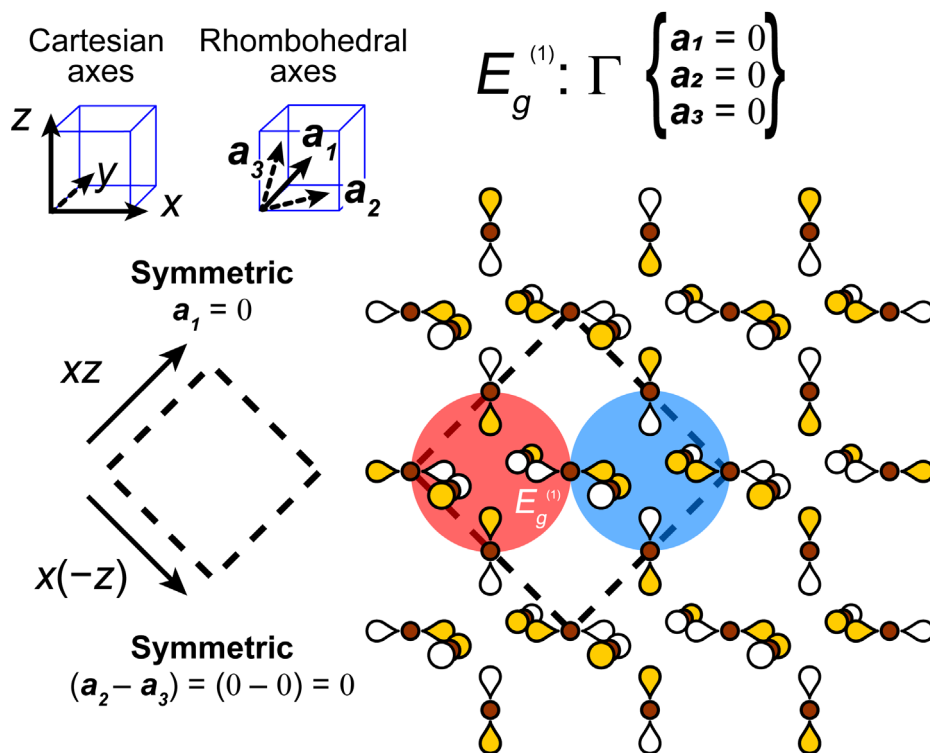


Figure S12. Derivation of the Bloch wave at Γ derived from the $E_g^{(1)}$ SALC (red circle). This Bloch wave is degenerate with the one shown in Figure S13 but is shown separately for ease of visualization.

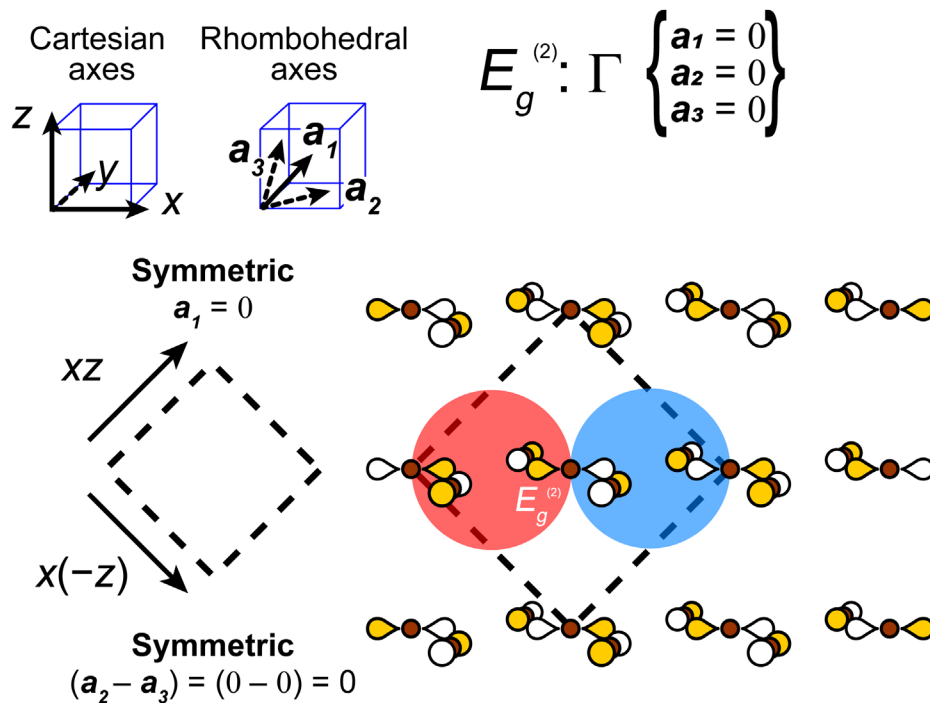


Figure S13. Derivation of the Bloch wave at Γ derived from the $E_g^{(2)}$ SALC (red circle). This Bloch wave is degenerate with the one shown in Figure S12 but is shown separately for ease of visualization.

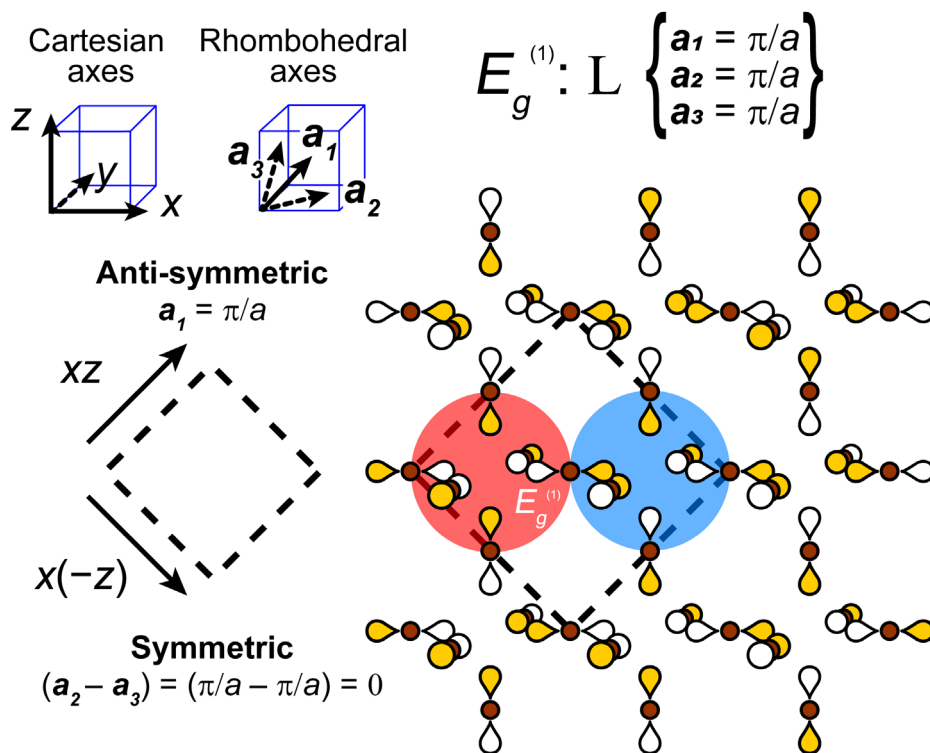


Figure S14. Derivation of the Bloch wave at L derived from the $E_g^{(1)}$ SALC (red circle). This Bloch wave is degenerate with the one shown in Figure S15 but is shown separately for ease of visualization.

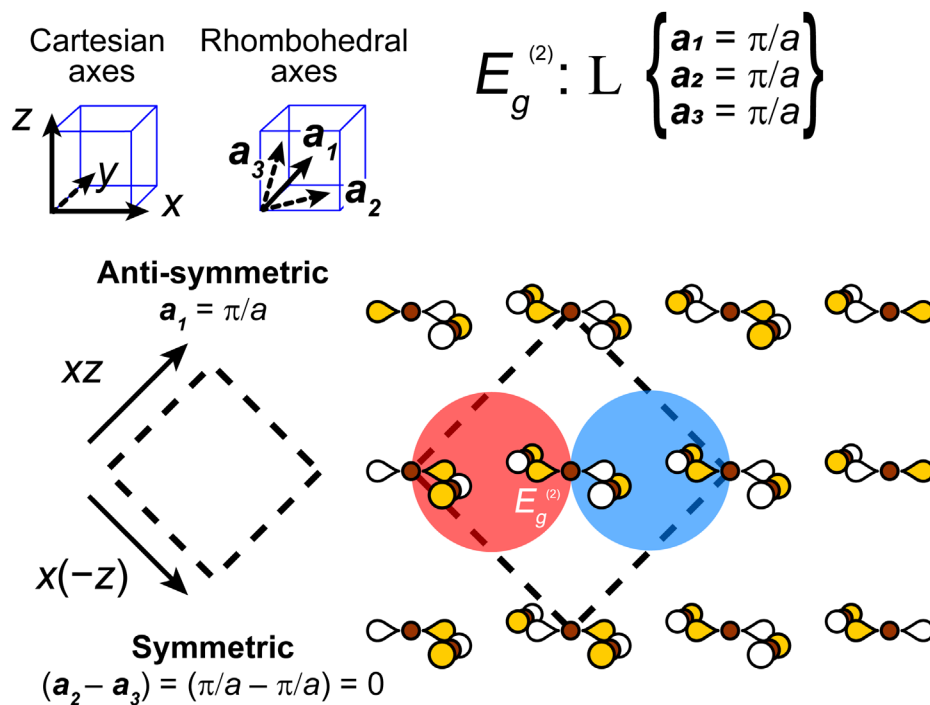


Figure S15. Derivation of the Bloch wave at L derived from the $E_g^{(2)}$ SALC (red circle). This Bloch wave is degenerate with the one shown in Figure S14 but is shown separately for ease of visualization.

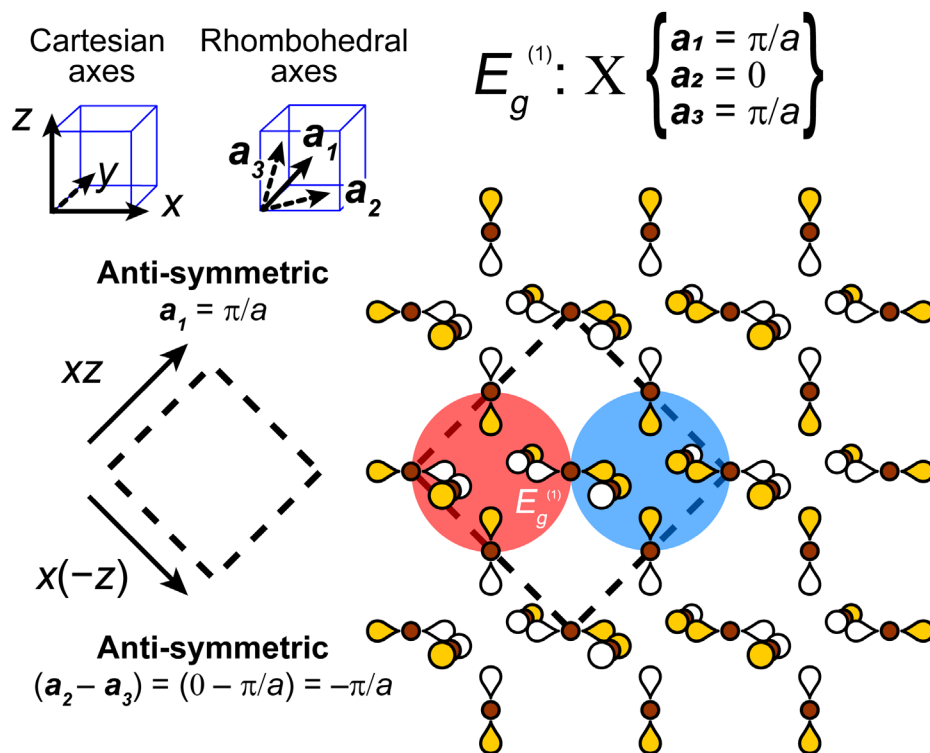


Figure S16. Derivation of the Bloch wave at X derived from the $E_g^{(1)}$ SALC (red circle). This Bloch wave is **not** degenerate with the one shown in Figure S17.

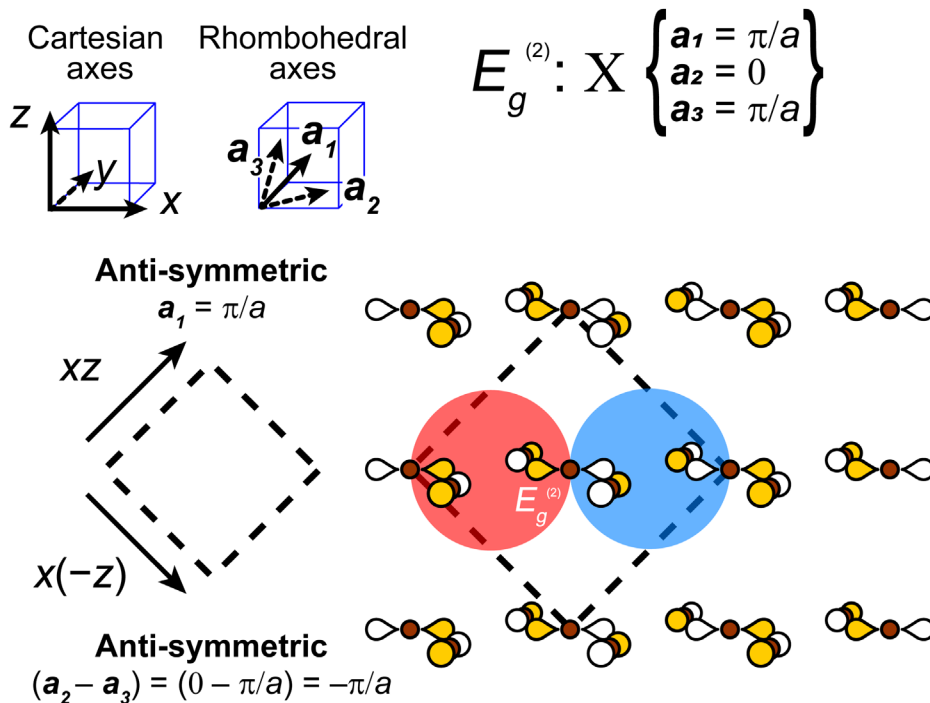


Figure S17. Derivation of the Bloch wave at X derived from the $E_g^{(2)}$ SALC (red circle). This Bloch wave is **not** degenerate with the one shown in Figure S16.

Analysis of halide-halide interactions

In situations where a metal-based atomic orbital cannot participate in a band (either because the metal is missing from the B/B' site or because the orbital's energy is too different in energy relative to that of the halides), the relative energies of the various \mathbf{k} points are determined by halide-halide interactions as shown for $\text{Cs}_2\text{Sn}\square\text{Br}_6$ in Section 3.2 in the main text. However, as discussed in Section 3.2, we must determine which halide-halide interactions are most important. The closest halide-halide contact is along the edge of the halide octahedron. However, the orbitals from these halides point towards the octahedral center and, therefore, have a 90° angle between them. This interaction (which we will call the 90° interaction) might be expected to be weak. The 180° interaction involving halides directly across the octahedron from one another involves p orbitals arranged for maximal overlap. However, these orbitals are a factor of $\sqrt{2}$ (~ 1.4 times) farther away. In the face of these competing factors, we have decided to determine the predominant interaction empirically. We do this by assuming that either the 90° interaction or the 180° interaction is the important one or that they both are equally important. We then determine the energetic order of SALCs for each case by looking at the net degree of bonding/antibonding (Figure S18).

We compare these predictions to DFT-generated band structures for materials in which one or both metal-based atomic orbitals do not participate in the valence/conduction band. In all cases, we find that considering only the 90° interaction gives predictions that agree with the DFT calculations, while considering the 180° or both the 90° and 180° give incorrect predictions. However, we should point out that most of the available DFT calculations are on bromide or iodide perovskites. It is possible that for lighter halides, the 180° interaction becomes more important. We expect that in fluorides and possibly some

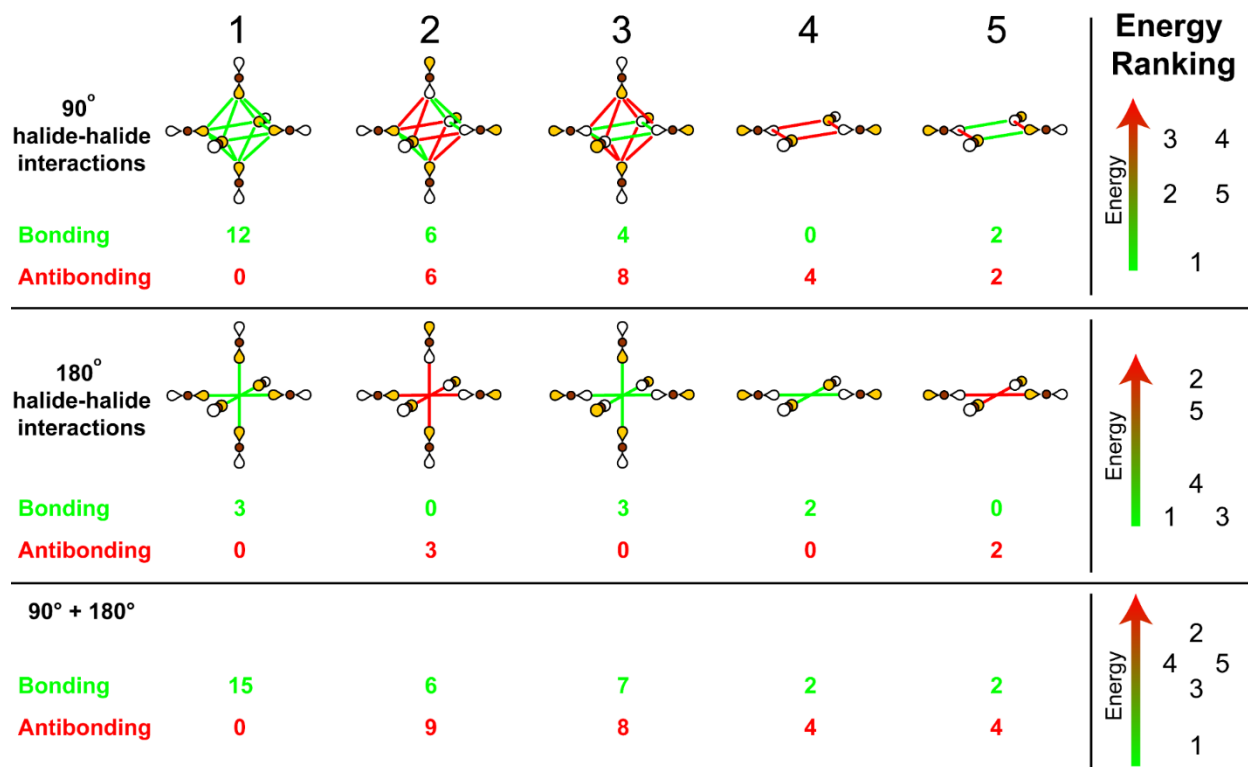


Figure S18. Analysis of the halide-halide bonding and antibonding interactions generated by the five possible configurations of p orbitals around a non-participatory metal site. The three scenarios consider only 90° interactions (**top**), only 180° interactions (**middle**) or equal 90° and 180° interactions (**bottom**). Empirically, we find that considering only 90° interactions gives the correct predictions.

chlorides, the 90° orbital overlap will be reduced (since the radial extension of the 2p/3p orbitals is less than in 4p/5p) and the 180° overlap increased (due to smaller lattice spacings).

Discussion of π -bonding bands

Derivation of π -bonding SALCs

We follow the same procedure for constructing π -bonding SALCs that we used for forming σ -bonding SALCs. Now we use the remaining twelve p orbitals that lie orthogonal to the metal halide σ -bonds as our basis set (Figure S19A). We must consider all twelve at once rather than two sets of six because the p_x and p_y orbitals (named assuming the p_z orbital points along the metal halide σ -bond) on each halide are related to one another by C_4 proper rotation axes and σ_d mirror planes. Our numbering scheme is given in Figure S19A. Decomposition of the orbital characters into their

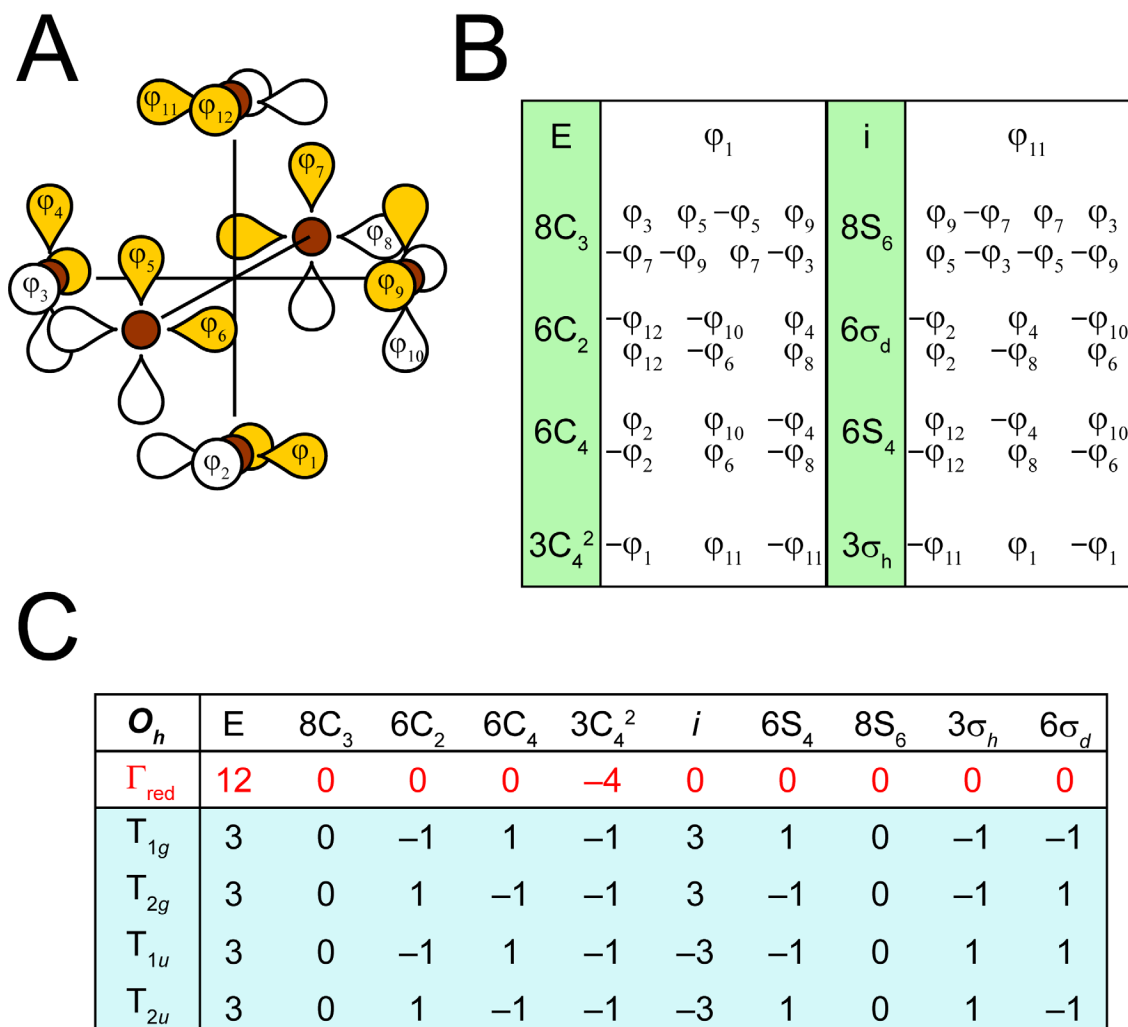


Figure S19. **A)** The octahedral arrangement of halide p orbitals, present in the double perovskite unit cell, used to construct the π -bonding SALCs. **B)** Projection table based on orbital φ_1 showing its relationships to the other orbitals in **A** under the symmetry operations of the O_h point group (green columns). **C)** Decomposition of the reducible representation for the orbitals in **A** into their irreducible representations (T_{1g} , T_{2g} , T_{1u} , & T_{2u}).

irreducible representations (Figure S19C) gives $\Gamma_{red} = T_{1g} + T_{2g} + T_{1u} + T_{2u}$, the expected representations for π orbitals in an octahedral ligand field.

To generate orbital pictures of these irreducible representations, we again apply the projection operator using the table given in Figure S19B. Since all four irreducible representations are triply degenerate, this can be done relatively easily by applying the projection operator to φ_1 , φ_2 , and a third orbital that is not involved in the first two representations. The resulting equations for each irreducible representation are shown below with the corresponding pictures given in Figure S20.

For the T_{1g} irreducible representation:

$$P_{T_{1g}}(\varphi_1) = \frac{1}{2} (\varphi_1 - \varphi_4 + \varphi_{10} + \varphi_{11}) \quad (11)$$

$$P_{T_{1g}}(\varphi_2) = \frac{1}{2} (\varphi_2 - \varphi_5 + \varphi_7 + \varphi_{12}) \quad (12)$$

$$P_{T_{1g}}(\varphi_6) = \frac{1}{2} (-\varphi_3 + \varphi_6 + \varphi_8 - \varphi_9) \quad (13)$$

For the T_{2g} irreducible representation:

$$P_{T_{2g}}(\varphi_1) = \frac{1}{2} (\varphi_1 + \varphi_4 - \varphi_{10} + \varphi_{11}) \quad (14)$$

$$P_{T_{2g}}(\varphi_2) = \frac{1}{2} (\varphi_2 + \varphi_5 - \varphi_7 + \varphi_{12}) \quad (15)$$

$$P_{T_{2g}}(\varphi_6) = \frac{1}{2} (\varphi_3 + \varphi_6 + \varphi_8 + \varphi_9) \quad (16)$$

For the T_{1u} irreducible representation:

$$P_{T_{1u}}(\varphi_1) = \frac{1}{2} (\varphi_1 + \varphi_6 - \varphi_8 - \varphi_{11}) \quad (17)$$

$$P_{T_{1u}}(\varphi_2) = \frac{1}{2} (\varphi_2 + \varphi_3 - \varphi_9 - \varphi_{12}) \quad (18)$$

$$P_{T_{1u}}(\varphi_5) = \frac{1}{2} (\varphi_4 + \varphi_5 + \varphi_7 + \varphi_{10}) \quad (19)$$

For the T_{2u} irreducible representations:

$$P_{T_{2u}}(\varphi_1) = \frac{1}{2} (\varphi_1 - \varphi_6 + \varphi_8 - \varphi_{11}) \quad (20)$$

$$P_{T_{2u}}(\varphi_2) = \frac{1}{2} (\varphi_2 - \varphi_3 + \varphi_9 - \varphi_{12}) \quad (21)$$

$$P_{T_{2u}}(\varphi_5) = \frac{1}{2} (-\varphi_4 + \varphi_5 + \varphi_7 - \varphi_{10}) \quad (22)$$

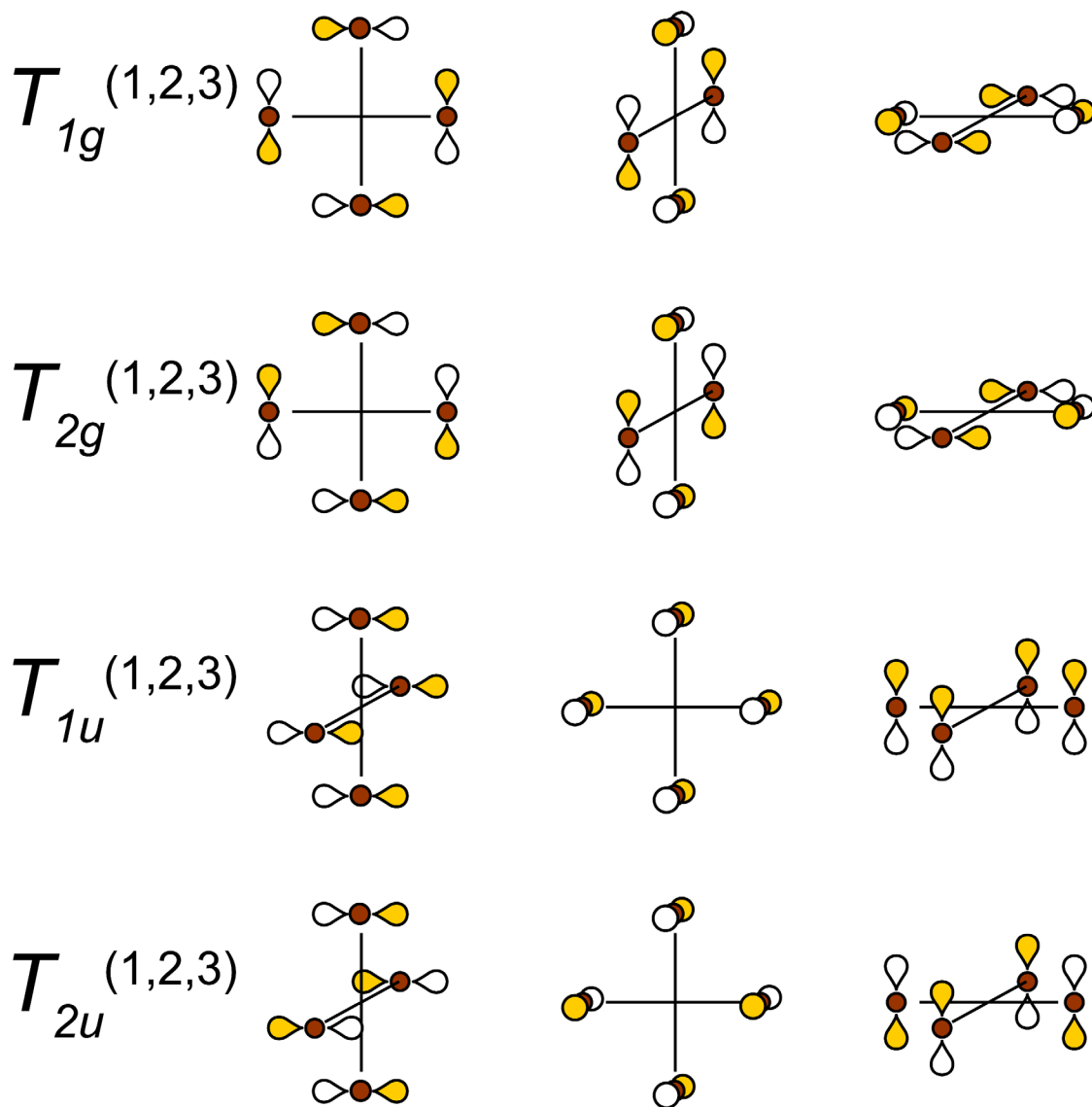


Figure S20. Representations of the π -bonding SALCs generated with the projection operator. Each representation is triply degenerate.

Halide-only Bloch waves derived from π -bonding SALCs

We use the same procedure to generate the π -bonding Bloch waves that we used for the σ -bonding ones (see main text and Figures S5-S17), translating each SALC in Figure S20 according to the symmetry dictated by the high-symmetry \mathbf{k} points Γ , \mathbf{L} , and \mathbf{X} . In lieu of showing each translation individually, we simply show the table of all 16 resulting Bloch waves in Figures S21 and S22. These are the π -bonding equivalents of the Bloch waves shown in Figure 5. The Bloch waves at Γ and \mathbf{L} shown in Figure S21 are constructed from one representation of each triply degenerate set. Two additional degenerate Bloch waves can be generated starting from the remaining two representations (not shown in Figure S21). The Bloch waves at \mathbf{X} in Figure S22 are split by translational symmetry giving a doubly degenerate and singly degenerate set. These are both shown in Figure S22. As in the σ -bonding case, the application of translational symmetry on the initial SALC in the B site determines the symmetry around the B' site. The

interaction of these Bloch waves with metal-centered orbitals was determined by inspection. In principle, the T_{1u} derived Bloch waves could interact with metal-centered p orbitals. However, from Figure S1, it is clear that the π T_{1u} set is predominantly non-bonding due to the existence of the more strongly interacting σ T_{1u} set. Therefore, potential interactions of the T_{1u} set with metal-centered p orbitals were excluded from Figures S21 and S22.

Prediction of band extrema in π -bonding bands.

To predict the band extrema in π -bonding bands (Table 1/Table S1), we use the same methods we used for σ -bonding. As in the σ -bonding case, we consider three possible scenarios: first, a band where metal-centered orbitals from both B and B' are involved, second a band where a metal-centered orbital from only the B site participates, and third, a band where no metal centered orbital is present. Only one set of metal orbitals (d_{xy} , d_{xz} , d_{yz}) is capable of π -bonding, simplifying the possibilities significantly. In the first case, where both the B and B' site contribute a $d_{xy}/d_{xz}/d_{yz}$ set, inspection of Figure S21/S22 shows two Bloch waves that match the $d_{xy}/d_{xz}/d_{yz}$ symmetry at both sites: a triply-degenerate wave at Γ and a singly degenerate wave at X (which only bonds with the d_{xy} metal orbitals). Both are derived from the T_{2g} irreducible

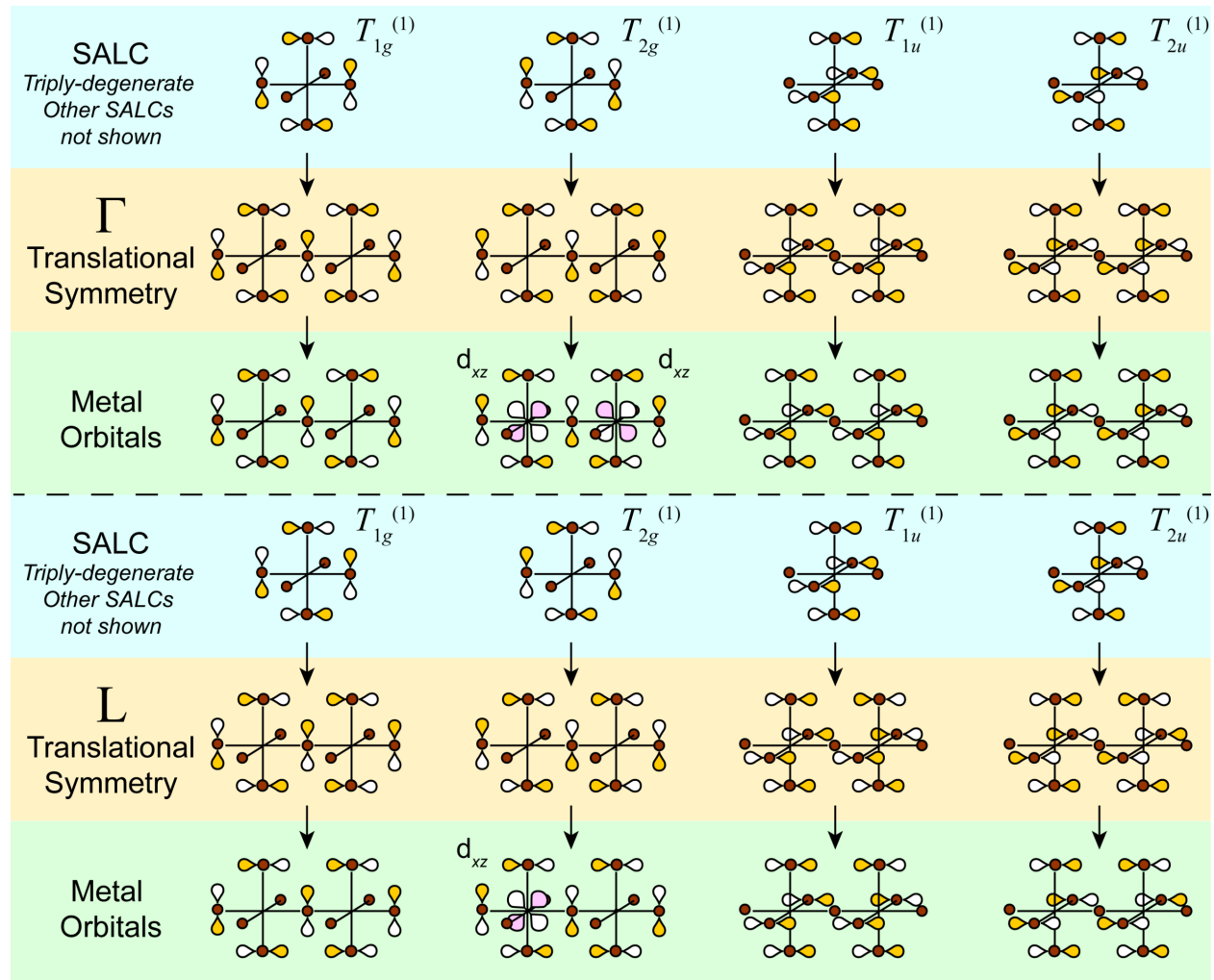


Figure S21. Summary of all possible Bloch waves based on the π -bonding SALCs at the high symmetry k points Γ , and L . Here, only one unit cell is shown, but all others will have the same symmetry. Only one of three degenerate Bloch waves (derived from one of the three degenerate starting SALCs) is shown in each instance.

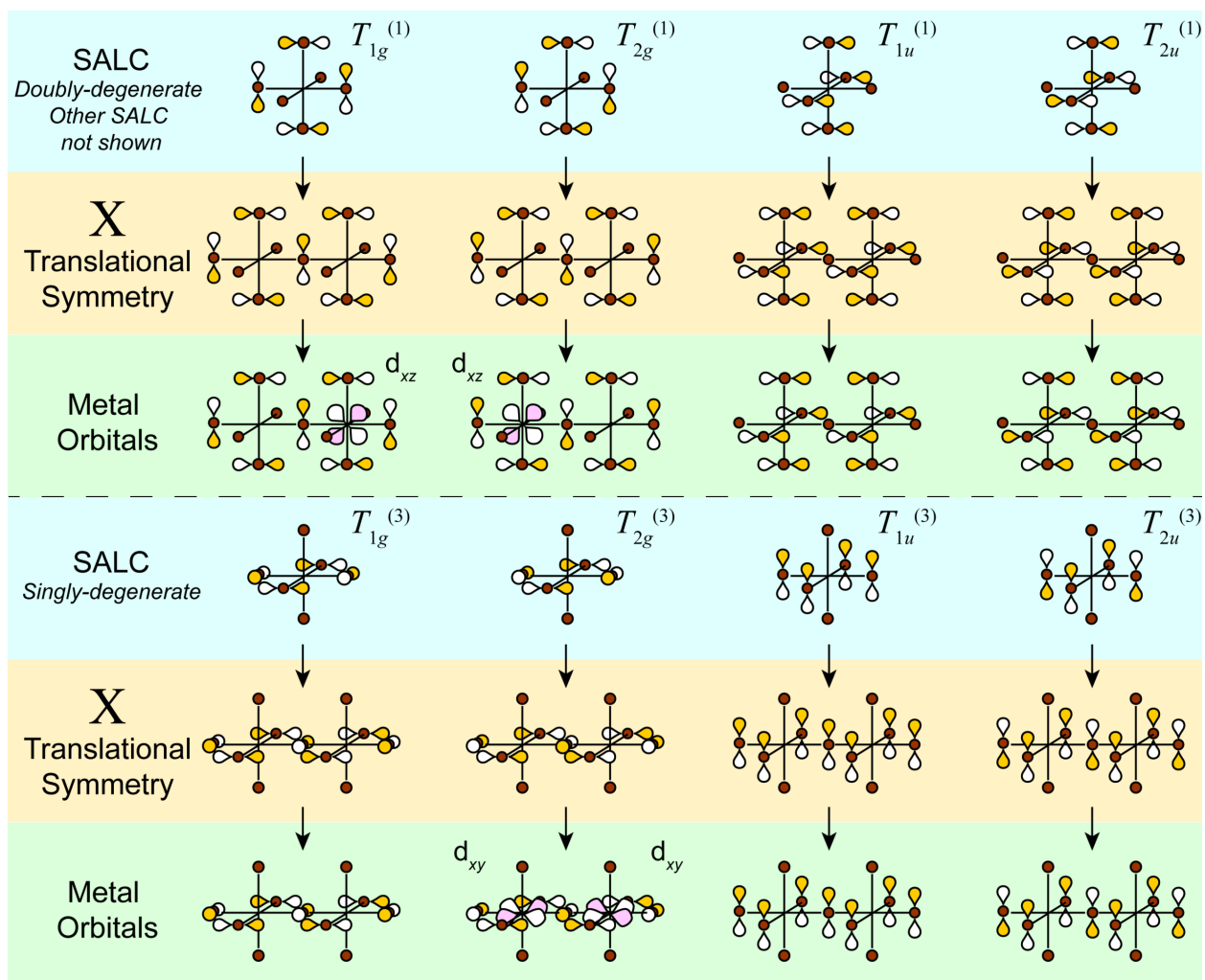


Figure S22. Summary of all possible Bloch waves based on the π -bonding SALCs at the high-symmetry \mathbf{k} point X . Here, only one unit cell is shown but all others will have the same symmetry. The originally triply degenerate sets split into doubly degenerate (top) and singly degenerate (bottom) sets due to the anisotropic translational symmetry at X .

representation. Following the logic we established in Section 3.1 in the main text, these two Bloch waves will be either the VBM (if the $d_{xy}/d_{xz}/d_{yz}$ orbitals are filled) or the CBM (if the orbitals are empty). This also implies that there will be a flat band from Γ to X since the B and B' d_{xy} orbitals participate in isoenergetic Bloch waves at both \mathbf{k} points. These results are summarized in Table S1.

In the second case, where only one B-site metal contributes a $d_{xy}/d_{xz}/d_{yz}$ orbital, we must turn again to halide-halide interactions to determine the relative energy of a band at the various \mathbf{k} points. The T_{2g} -derived Bloch waves at all \mathbf{k} points and the doubly degenerate T_{1g} -derived set at X can all interact with at least one metal-centered $d_{xy}/d_{xz}/d_{yz}$ orbital and all generate regions which permit 90° X – X interactions (Figure S23). In these regions, the 90° halide-halide interactions occur over the same distance they did in the σ Bloch waves (neglecting the typically small differences between B – X and B' – X bond lengths) and therefore have effects of a similar magnitude. To find the VBM, we must find which of these Bloch waves has the most antibonding arrangement of 90° halide-halide interactions. For the VBM, this is the doubly degenerate set at X derived from T_{2g} . The CBM will be the Bloch wave with the most bonding arrangement. For the CBM, this is both the singly degenerate T_{2g} -derived set at X and the triply degenerate T_{2g} -derived set at Γ . Again,

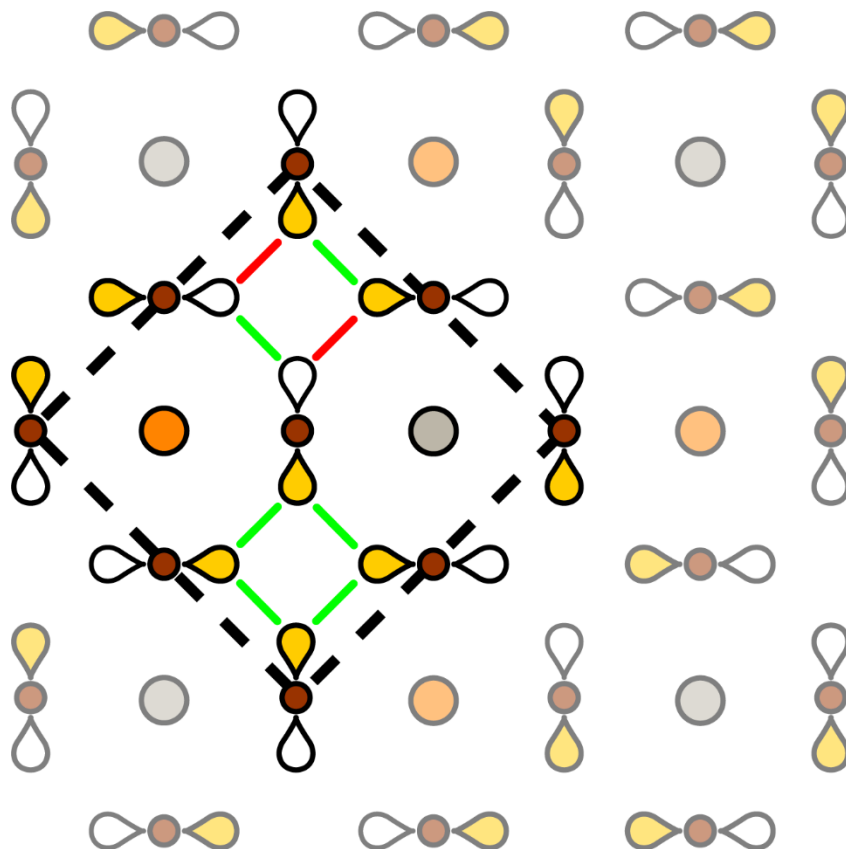


Figure S23. Example of halide-halide interactions in a π -bonding Bloch wave. The green and red colored lines show 90° halide-halide bonding and antibonding interactions, respectively. The example shown is the Bloch wave at L derived from one of the T_{2g} SALCs.

this implies that the conduction band should be flat, or nearly so, from Γ to X . These results are summarized in Table S1. Consistent with our prediction, DFT calculations of Cs_2HfI_6 ,⁹ and of Cs_2TiI_6 ,¹⁰ which have $d_{xy}/d_{xz}/d_{yz}$ based conduction bands, show the Γ and X conduction band minima lie within 0.02 eV and 0.07 eV, respectively, of each other.

There is one case left to examine: the non-bonding situation where no metal orbital participates in the π band. From the MO diagram in Figure S1, we can see that this situation will only be relevant for the valence band and only when a d^0 metal is present. As discussed above, we look for the Bloch waves with the most antibonding configuration of 90° halide-halide interactions. The Bloch waves derived from T_{1u} and T_{2u} are incapable of these interactions, so we discount them. Of the remaining Bloch waves, the total 90° antibonding configuration is found at Γ and the singly degenerate set at X (derived from the T_{1g} set).

While the analysis we have just presented is fairly straightforward, there are two issues that can complicate accurate determination of band extrema when $d^0 - d^9$ cations (and therefore π -bonding bands) are involved.

Table S1. Expected k points of the conduction band minimum (CBM) and valence band maximum (VBM) for all possible combinations involving a π -bonding band. Note that the VBM and CBM should be evaluated independently.

Orbitals		Prediction	
B	B'	VBM	CBM
$d_{xy}/d_{xz}/d_{yz}$	$d_{xy}/d_{xz}/d_{yz}$	X & Γ	X & Γ
$d_{xy}/d_{xz}/d_{yz}$	null	X	X & Γ
null	null	X & Γ	–

The first is the tendency of metals with partially occupied degenerate orbitals to undergo spontaneous Jahn-Teller distortions which relieve the orbital degeneracy and break the cubic symmetry of the material. While extension of the theory to non-cubic systems is possible, it is beyond the scope of this work.

The second issue is important when the double perovskite contains one $d^0 - d^9$ cation and one main group or d^{10} cation. The main group and d^{10} cations have HOMOs and LUMOs based on σ -bonds while the $d^0 - d^9$ cation will have π -bonding character as a component of either its HOMO or LUMO. Because the π - and σ -bonding are based on orthogonal sets of halide-p orbitals they cannot mix even if their electronic states have the same energy, making this a case of accidental degeneracy. Therefore, if both π and σ manifolds are potentially present near the band edges, some knowledge of the relative energies of the metal orbitals is necessary to determine the correct band extrema. A good example of this is the conduction band of $\text{Cs}_2\text{AgYCl}_6$ where one of the lowest conduction bands is based on the Ag 5s orbital and another is based on the Y $3d_{xy}/3d_{xz}/3d_{yz}$ set.¹¹ These bands cross without mixing and it is necessary to know that the Ag 5s band is lower in energy to predict the CBM correctly. For a more complete discussion of this example, see Reference 9.

Discussion of the electronic structure of $\text{Cs}_2\text{MBiCl}_6$ (M = Na, K)

As noted in Table 2, there is a small amount of alkali p character present in the conduction band of $\text{Cs}_2\text{MBiCl}_6$ (M = Na, K; Figures S24-S25). The appearance of this p character is unexpected since the lowest unoccupied orbital should be the Na 3s or K 4s. Overall, this contribution is small and we suspect it originates from sp-mixing of the Na 3s (K 4s) with either the filled Na 2p (K 3p) or the empty Na 3p (K 4p). This alkali p character is present only near Γ which, since the other metal orbital involved in the band is the Bi 6p, is consistent with the prediction of Figure 5. Table 1 predicts that, given the orbital contributions (Bi 6p/M p), the CBM will be at Γ while if the alkali p character is absent (Bi 6p/null) the CBM will be at **L**. In the DFT-calculated structures in Figures S24-S25, we observe that the energies of the conduction band at Γ and **L** are within ca. 0.1 eV of one another, too close to reliably distinguish between them. Therefore, we suggest that the appearance of low levels of alkali p character in the conduction band is responsible for the flatness of the $\text{Cs}_2\text{MBiCl}_6$ conduction band from Γ to **L**. However, closer study would be required to confirm this.

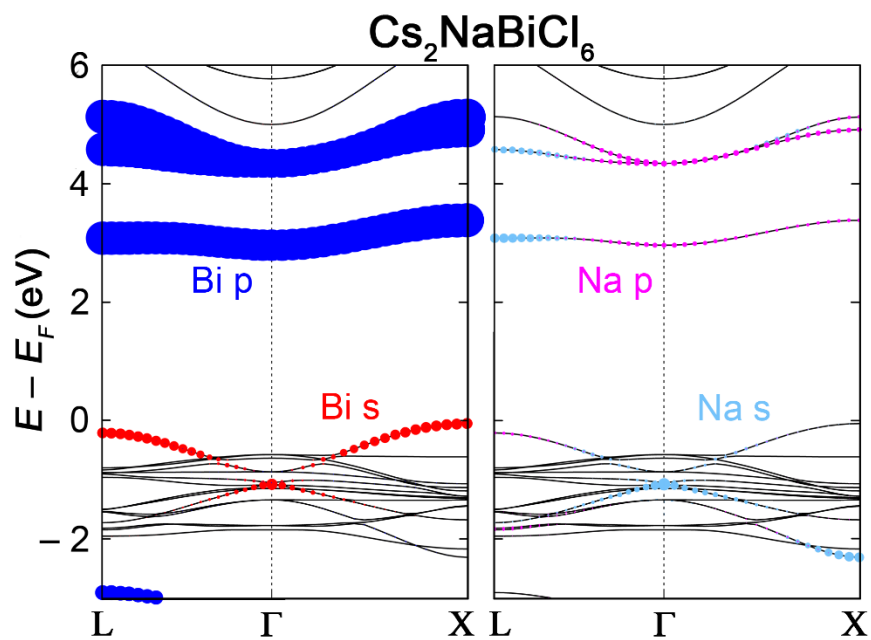


Figure 24. Band structure of the double perovskite Cs₂NaBiCl₆ computed with DFT. The band structure is shown in duplicate and the orbital contributions of the B-site atoms (Na and Bi) are given in color with the size of the dots proportional to the size of the contribution. Halide contributions are also present but have been omitted for clarity.

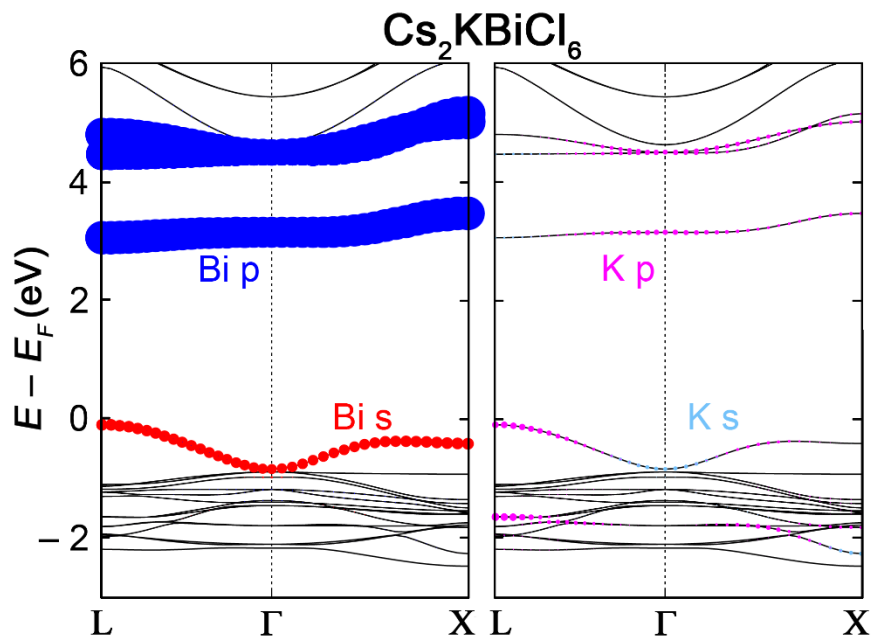


Figure 25. Band structure of the double perovskite Cs₂KBiCl₆ computed with DFT. The band structure is shown in duplicate and the orbital contributions of the B-site atoms (K and Bi) are given in color with the size of the dots proportional to the size of the contribution. Halide contributions are also present but have been omitted for clarity.

References

- (1) (a) Hoffmann, R. *Solids and Surfaces: A Chemist's View of Bonding in Extended Structures*; **1988**, Wiley-VCH; (b) Ashcroft, N. W.; Mermin, N. D. *Solid State Physics*; **1976**, Holt, Rinehart, and Winston; (c) Harrison, W. A. *Electronic Structure and the Properties of Solids*; **1980**, W. H. Freeman.
- (2) (a) Kresse, G.; Hafner, J. *J. Phys. Condens. Matter* **1994**, *6*, 8245; (b) Kresse, G.; Furthmüller, J. *Phys. Rev. B* **1996**, *54*, 11169.
- (3) Csonka, G. I.; Perdew, J. P.; Ruzsinszky, A.; Philipsen, P. H. T.; Lebègue, S.; Paier, J.; Vydrov, O. A.; Ángyán, J. G. *Phys. Rev. B* **2009**, *79*, 155107.
- (4) Slavney, A. H.; Hu, T.; Lindenberg, A. M.; Karunadasa, H. I. *J. Am. Chem. Soc.* **2016**, *138*, 2138.
- (5) Ketelaar, J. A. A.; Rietdijk, A. A.; van Staveren, C. H. *Recl. Trav. Chim. Pays-Bas* **1937**, *56*, 907.
- (6) Morris, L. R.; Robinson, W. R. *Acta Crystallogr., Sect. B* **1972**, *28*, 653.
- (7) Kresse, G.; Joubert, D. *Phys. Rev. B* **1999**, *59*, 1758.
- (8) Connor, B. A.; Leppert, L.; Smith, M. D.; Neaton, J. B.; Karunadasa, H. I. *J. Am. Chem. Soc.* **2018**, *140*, 5235.
- (9) Kang, B.; Biswas, K. *J. Phys. Chem. C* **2016**, *120*, 12187.
- (10) Ju, M.-G.; Chen, M.; Zhou, Y.; Garces, H. F.; Dai, J.; Ma, L.; Pature, N. P.; Zeng, X. C. *ACS Energy Lett.* **2018**, *3*, 297.
- (11) Du, M.-H.; Biswas, K. *J. Lumin.* **2013**, *143*, 710.